Thickness Dependent Properties in Oxide Heterostructures Driven by Structurally Induced Metal–Oxygen Hybridization Variations

Zhaoliang Liao, Nicolas Gauquelin, Robert J. Green, Sebastian Macke, Julie Gonnissen, Sean Thomas, Zhicheng Zhong, Lin Li, Liang Si, Sandra Van Aert, Philipp Hansmann, Karsten Held, Jing Xia, Johan Verbeeck, Gustaaf Van Tendeloo, George A. Sawatzky, Gertjan Koster, Mark Huijben, and Guus Rijnders*

Thickness-driven electronic phase transitions are broadly observed in different types of functional perovskite heterostructures. However, uncertainty remains whether these effects are solely due to spatial confinement, broken symmetry, or rather to a change of structure with varying film thickness. Here, this study presents direct evidence for the relaxation of oxygen-2p and Mn-3d orbital (p–d) hybridization coupled to the layer-dependent octahedral tilts within a $La_{2/3}Sr_{1/3}MnO_3$ film driven by interfacial octahedral coupling. An enhanced Curie temperature is achieved by reducing the octahedral tilting via interface structure engineering. Atomically resolved lattice, electronic, and magnetic structures together with X-ray absorption spectroscopy demonstrate the central role of thickness-dependent p–d hybridization in the widely observed dimensionality effects present in correlated oxide heterostructures.

1. Introduction

A diverse range of phenomena spanning from colossal magnetoresistance to metal-to-insulator transition (MIT) and superconductivity have been attracting tremendous interest in transition metal oxides (TMOs) for both fundamental research as well as technological applications.[1] Of particular interest are the phase transitions in TMOs, which can be manipulated by tuning either bandwidth or band-filling.[2,3] Various phase transitions (MIT, ferroelectricity to paraelectricity, ferromagnetic to antiferromagnetic) can already be achieved in different types of TMO heterostructures just by varying the thickness.[4–10] In recent literature, several physical models are used as a design principle in order to achieve control over the reconfigurable properties by changing the thickness. The reduced dimensionality tipping the delicate competition between collective quantum phases which are proposed to contribute to the MIT in ultrathin $LaNiO_3$ and $SrVO_3$ thin films[4–6] are very well-known examples of thickness effects on properties, while a polar catastrophe is proposed to generate a magnetic phase transition in polar $LaMnO_3$ ultrathin films.[7]

The recently revealed nontrivial oxygen octahedral coupling at perovskite oxide interface which induces the modulation of oxygen coordination across the interface should play an important role in affecting the delicate spin–charge–orbital coupling in those correlated heterostructure systems.[11–15] Scanning transmission electron microscopy (STEM) using the latest scanning and imaging techniques for both $SrRuO_3$[12] and $La_{2/3}Sr_{1/3}MnO_3$ (LSMO)[13] clearly shows a thickness dependent oxygen coordination and resultant modified spin–orbital coupling. Our previous study further suggests that a reduced

Dr. Z. L. Liao, Dr. L. Li, Prof. G. Koster, Prof. M. Huijben, Prof. G. Rijnders
MESA+ Institute for Nanotechnology
University of Twente
7500 AE, Enschede, The Netherlands
E-mail: m.huijben@utwente.nl

Dr. N. Gauquelin, J. Gonissen, Prof. S. van Aert, Prof. J. Verbeeck, Prof. G. Van Tendeloo
Electron Microscopy for Materials Science (EMAT)
University of Antwerp
2020 Antwerp, Belgium

Dr. R. J. Green, Dr. S. Macke, Prof. G. A. Sawatzky
Quantum Matter Institute and Department of Physics and Astronomy
University of British Columbia
2355 East Mall, Vancouver V6T 1Z4, Canada

Dr. R. J. Green
Max Planck Institute for Chemical Physics of Solids
Nöthnitzerstraße 40, 01187 Dresden, Germany

Dr. S. Macke, Dr. Z. Zhong, Dr. P. Hansmann
Max Planck Institute for Solid State Research
Heisenbergstraße 1, 70569 Stuttgart, Germany

Dr. S. Thomas, Prof. J. Xia
Department of Physics and Astronomy
University of California, Irvine
Irvine, CA 92697, USA

Dr. Z. Zhong, Dr. L. Si, Prof. K. Held
Institute of Solid State Physics
TU WIEN
A-1040 Vienna, Austria

DOI: 10.1002/adfm.201606717

octahedral distortion is corresponding to an increased Curie temperature in LSMO films.[13] Given the close similarity of the structures in the previously mentioned examples[4–10] with these latter systems,[12,13] the question arises whether a similar structural effect could be essential in the former studies and how is the structure coupled to spin–charge–orbital degrees of freedom in giving rise to those emergent phenomena. The missing link is an exact physical relationship between the observed modified structure, the changes of electronic structure, and the underlying physical phenomena for these thickness driven phase transitions. Here, we provide experimental evidence for the structure–property relationship in an epitaxial model system, LSMO on $NdGaO_3$ (NGO), where orbital hybridization is identified as the main driving mechanism for thickness dependent property changes. By reducing the octahedral tilting and hence increasing the p–d hybridization via interfacial structure engineering, ferromagnetism can be stabilized and an increased Curie temperature is achieved. It is very plausible that similar effects play a role in other oxide heterostructures and can be used as a leading design principle crucial for further development of these functional heterostructures into miniaturized oxide electronic devices.

The half metallic ferromagnet LSMO is of great importance due to its 100% spin polarized nature[16,17] and is a promising material for oxide spintronic applications. For LSMO thin films, previous studies have already shown that the ferromagnetic behavior severely depends on the film thickness.[10,18–24] Tremendous efforts have been made to unravel this thickness dependence, but its origin is still debated.[10,18–27] The variation of Mn^{3+}/Mn^{4+} ratio, orbital reconstruction due to strain and/or broken symmetry together with extrinsic structure imperfection due to growth are several proposed mechanisms responsible for this deterioration of ferromagnetism.[18–25] Preference of either $3z^2–r^2$ or $x^2–y^2$ occupation is suggested to favor an antiferromagnetic ground state,[18,19,28,29] while the enrichment of Mn^{3+} would also enhance Jahn–Teller distortions.[23,24] However, an interfacial charge transfer limited to ≈0.13 eV and confined to ≈2 unit cells (uc)[30] cannot explain the long range thickness dependence in thicker films, although crucial for local magnetism.[25] Also the observed ferromagnetic behavior of $La_{1-x}Sr_xMnO_3$ (with $T_C > 250$ K) over a wide range of compositions $0.15 < x < 0.5$[16] indicates the limited impact of any possible charge transfer on the Curie temperature. A roughly <3 uc length scale of charge leakage as demonstrated in $(LaMnO_3)_{2n}/(SrMnO_3)_n$ superlattice should further suppress the impact of charge transfer.[31]

In addition, possible changes in the overlap of the orbitals due to structural changes were disregarded up to now, although a strong correlation with magnetic behavior has been demonstrated in bulk manganites.[3,32,33] Recently it has been shown that the oxygen octahedral rotation pattern in LSMO films can be tuned by direct coupling to the oxygen octahedral rotation pattern of the underlying substrate.[13] NGO substrates provide a specific octahedral tilt angle, and corresponding orbital overlap, which can be reduced by an increased thickness of the LSMO layer as well as by incorporation of a $SrTiO_3$ (STO) buffer layer. In the present study, we will unravel the correlation between the orbital overlap and the thickness dependence by systematically investigating the relation between magnetic behavior, crystal structure, orbital reconstruction, and bandwidth in LSMO films of various thicknesses using buffered and capped samples. Our results demonstrate the dominating role of the local O-2p and Mn-3d (p–d) orbital hybridization to the ferromagnetic ordering at the atomic scale in LSMO films and they reveal that spatial variation in p–d orbital hybridization, due to octahedral relaxation within LSMO, is responsible for the observed thickness dependence in material properties.

2. Results and Discussion

LSMO thin films were grown by pulsed laser deposition on $NdGaO_3$ (110) (NGO) substrates (see Experimental Section). Control over the near-interfacial crystal structure was achieved by atomically precise thickness control and the use of ultrathin buffer and capping layers, or combinations thereof, which will hereafter be referred to as BL and CL, respectively,[13] thereby inducing the hypothesized variation of the orbital overlap in LSMO films. The oxygen octahedral rotation pattern across a 20 uc LSMO/NGO (L_{20}/NGO) interface was imaged by annular bright field STEM (ABF-STEM) (see **Figure 1**a). The MnO_6 octahedra are shown to follow the tilt angle of NGO in the interface region due to the oxygen octahedral coupling (OOC) effect,[11,13] which progressively decays away from the interface and is already negligible in the 4th uc. Figure 1b shows the profile of projected B—O—B bond angle θ in (001) plane, which is determined using statistical parameter estimation theory[34,35] (see Figure S1 in the Supporting Information). The bond angle θ in LSMO right at the interface is comparable to the angle in the NGO substrate (= 165°) and increases, starting from the interface, up to a saturation value of ≈173° above the 4th LSMO uc. Further away from the interface, a long range slow relaxation tail of the octahedral rotation pattern should exist, similar to LSMO/STO heterostructures.[26]

The existence of a slow relaxation tail is evidenced by an increasing out-of-plane lattice parameter c with increasing film thickness, as shown in Figure 1c (for the measurement of c, see Figure S2 in the Supporting Information). Additionally, upon the introduction of a STO BL, which renders the octahedral rotation pattern in the LSMO film to behave like bulk already starting from the interface (see ref. [13] and Figure S3 in the Supporting Information), the lattice constant c is increased (see Figure 1c). For example, the increased lattice constant c of a L_{30}/S_6 film becomes almost identical to that of a nonbuffered 90 uc LSMO (L_{90}). Note that the buffered LSMO films possess the same in-plane lattice constant as the nonbuffered LSMO films, as confirmed by the reciprocal space mapping (see Figure S2 in the Supporting Information). On the other hand, introducing a STO CL does not change the LSMO lattice constant (see Figure 1c), in contrast to a STO BL. From the observed structural effects, we can infer that an increase of the lattice constant c due to increasing thickness or induced by a STO BL seems to suggest that the presence of a long range structural relaxation is more likely caused by interface OOC rather than strain accommodation.

The relationship between structure and measured magnetic properties is investigated by using the variation of T_C for films with different thicknesses of LSMO and presence/absence of a

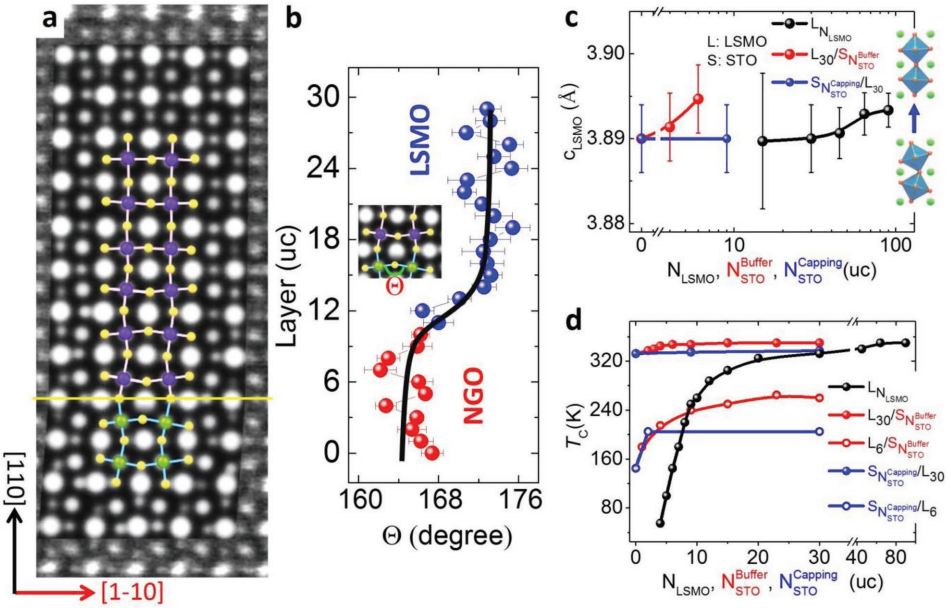

Figure 1. Relaxation of octahedra induced thickness-properties correlation. a) ABF-STEM image of LSMO/NGO cross-section. The intensity (I) is rescaled to $-I^{1/4}$ for better oxygen contrast. Inset is the refined parametric model using statistical parameter estimation. The colorized atoms and bonds highlight the relaxation of octahedral and B—O—B bond angle. b) The layer position dependent [1–10] directional and (001) plane projected B—O—B bond angle θ. Inset shows the definition of θ. c,d) The LSMO out-of-plane lattice constant and Curie temperature T_C of LSMO films as a function of thickness of LSMO (N_{LSMO}), STO buffer layer ($N^{Buffer}{}_{STO}$), and capping layer ($N^{Capping}{}_{STO}$).

STO BL/CL as shown in Figure 1d. Parallel to the octahedral rotation happening at the direct proximity to the interface in LSMO discussed above, T_C is dramatically reduced in ultrathin LSMO, e.g., down to 50 K for a 4 uc LSMO film (see Figure 1d). With increasing thickness without variation of the OOC effect, the T_C increases and is promoted to its bulk value of 350 K in relatively thick films (>30 uc).

Interestingly, films with a larger out-of-plane lattice constant have a higher T_C (see Figure 1c,d). In accordance, the increased lattice constant c of a 30 uc LSMO film by a STO BL corroborates with a T_C increase from 332 K to 350 K. In contrast, the presence of a STO CL does not influence the T_C (L_{30} vs S_9/L_{30}), where it was already observed that the structure of the LSMO was not affected. The difference between the effect of BL and CL on magnetism again suggests a pivotal role of octahedral tilt in the magnetism of the LSMO films. A record recovery of T_C by ≈120 K was observed for buffered 6 uc LSMO films (L_6/S_{23}) (see Figure 1d), consistent with the significant reduction of the octahedral tilt in LSMO by such STO BL.[13]

A more detailed investigation of the role of the STO BL on magnetization and transport is shown in **Figure 2**. In addition to the enhancement of T_C, the saturated magnetic moment (M_S) is increased when a STO BL is present (see Figure 2a). Reduced saturated magnetism in the L_6 film compared to bulk (e.g., L_{90}) is mainly due to the presence of a structural distortion near the interface and the existence of a surface magnetic dead layer.[13] This surface dead layer can be reduced by introducing a STO CL. Figure 2a shows that both the nonbuffered and buffered 6 uc LSMO films exhibit a higher saturated magnetic moment after the introduction of a 2 uc STO CL. For the $S_2/L_6/S_9$ film, the M_S is equal to 3.4 μ_B/Mn at 25 K, close to the value (≈3.7 μ_B/Mn) in bulk films,[36] indicating the absence of a magnetic dead layer. The CL significantly increases the T_C of nonbuffered ultrathin LSMO films (e.g., S_2/L_6) whereas it has just a minor impact on the T_C of buffered LSMO films (e.g., $S_2/L_6/S_9$) (see Figure 2a) and almost no effect on the T_C of thick LSMO (e.g., S_9/L_{30}) (see Figure 1d). This indicates a very local effect of the CL on the topmost layers of the films. The increased magnetism with increasing thickness of the BL suggests a gradual structure relaxation within the STO layers. In addition to this stabilized magnetism, the buffered LSMO films exhibit a higher conductivity (see Figure 2b). These modifications of magnetic and electrical properties, through capping, buffering, and thickness variations, point to the importance of structure relaxation in these thickness driven phenomena.

To ensure that this enhancement of ferromagnetism is exclusively caused by the presence of a STO BL/CL, a 6 uc LSMO sample with a patterned STO BL and CL is fabricated (see Figure 2c for schematic; for the STO patterning-process, see Figure S4 in the Supporting Information). Left- and right-circularly polarized light is focused on the LSMO layer and reflected. The phase difference between the two polarizations is measured using a scanning Sagnac Interferometer.[37] This enables the mapping of the Kerr intensity, indicating three distinguishable regions with different magnetic properties (see Figure 2c). In the Kerr map, the Curie temperatures for the different regions were determined from the temperature dependent Kerr signal (θ_K) as shown in Figure 2d. T_C is determined from the second derivative of the Kerr signal (see Figure S5 in the Supporting Information). T_C for region A (S_2/L_6), B (L_6), and C (L_6/S_3) are 191, 135, and 213 K, respectively, which are quite consistent to values determined by vibrating sample magnetometry (VSM) shown in Figure 1d. This experimental result unambiguously

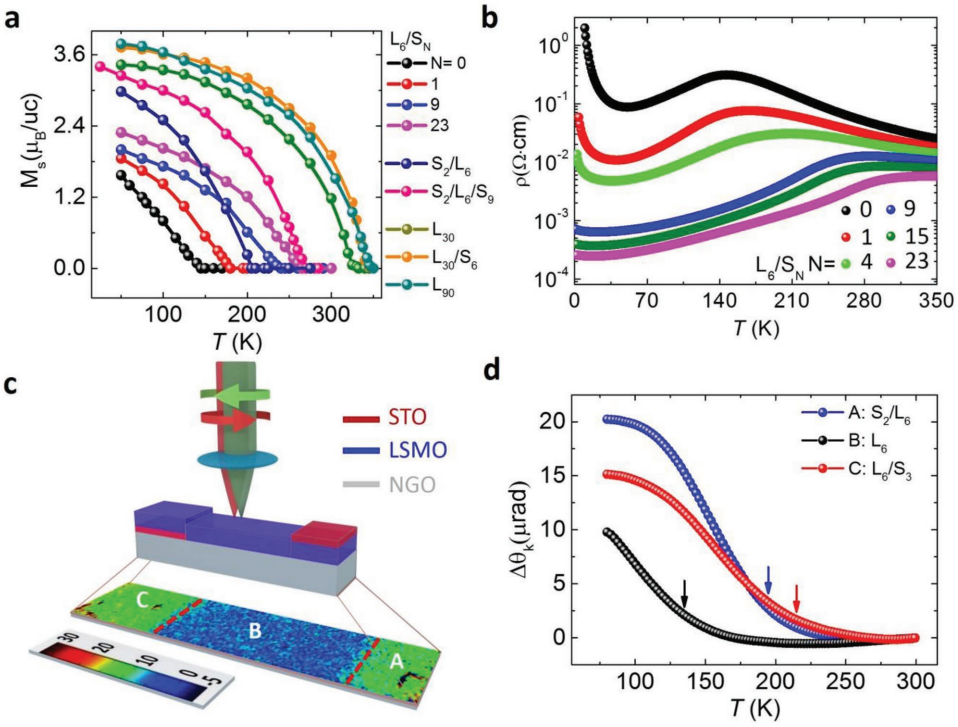

Figure 2. Impact of STO buffer and capping layers on magnetic and transport properties of LSMO films. a) Temperature-dependent saturated magnetization for different thicknesses of LSMO films with/without STO buffer/capping layers. b) Temperature-dependent resistivity for 6 uc LSMO films with different thickness of STO buffer layer. c) Kerr signal mapping of a patterned 6 uc LSMO film with size of 4.5 × 1 mm^2. The thicknesses of the STO buffer and capping layers are respectively 3 and 2 uc. d) Temperature-dependent Kerr signal at region A (S_2/L_6), region B (L_6), and region C (L_6/S_3). The arrows indicate the Curie temperature (T_C).

demonstrates the enhancement of ferromagnetism due to STO BL and CL, fully excluding sample to sample variation.

We now turn to the vertical distribution of magnetism in the layers. For that purpose we determined a depth resolved magnetic profile probed by synchrotron resonant soft X-ray reflectivity (RSXR)[38] (see Figure S6 in the Supporting Information). Without CL, both the buffered and nonbuffered 6 uc LSMO films showed a magnetic dead layer near the top surface of LSMO layers (see **Figure 3**a,b). This suggests that the STO BL apparently is able to increase the overall Curie temperature, but cannot remove the surface dead layer. Yet the surface dead layer was absent when the sample was capped with STO, both for the buffered and nonbuffered LSMO films, see Figure 3c,d. This enhanced magnetism due to the STO CL revealed by RSXR was consistent with the earlier described magnetization measurement using VSM (see Figure 2a). From the RSXR, one can extract a stoichiometry profile for both buffered and nonbuffered LSMO films, verifying their similarities and sharp chemical contrast across interfaces. RSXR also reveals a stoichiometric profile from interface to bulk region except the top surface. The variation of the La/Sr stoichiometry near the top surface is probably important to explain the role of the CL, since the capped samples have a more stoichiometric surface than noncapped samples (see Figure 3). An enhanced surface structural distortion, as indicated by our DFT calculation (see the Supporting Information), may also play a strong role in inducing a surface dead layer, while a STO CL will recover surface magnetism by reducing the surface distortion, similar to observations for $LaNiO_3$ films.[39]

Having established a strong connection of the magnetism to the local structure at or near heterointerfaces, we now turn to investigate any role that orbital reconstruction might play. Based on an orbital reconstruction model,[18,19,28] a stronger $3z^2$–r^2 orbital reconstruction is expected with an increased c/a ratio which favors C-type antiferromagnetism, degrading ferromagnetism in L_{30}/S_6 films as compared to L_{30} films. To quantify how the orbital reconstruction could influence the magnetism in LSMO, the Mn $3z^2$–r^2 and x^2–y^2 orbitals were preferentially probed by in-plane (σ) and out-of-plane (π) polarized X-ray absorption spectroscopy (XAS) respectively at the Mn $L_{2,3}$ edge (see **Figure 4**a). The measured XAS is shown in top panel of Figure 4b. For different films, their two spectra I_σ and I_π all show slight difference, indicating a small linear dichroism. The X-ray linear dichroism (XLD) is calculated as the intensity difference between the signals with different polarization ($I_\sigma - I_\pi$). As shown in the bottom panel of Figure 4b, all films exhibit quite similar XLD characteristics, e.g., L_6 and L_6/S_9 on the one hand; L_{30} and L_{30}/S_6 on the other hand. The relative $3z^2$–r^2 to x^2–y^2 orbital occupancy can be quantified using sum-rules of the XLD spectra, where the ALD percentage is defined by the integrated linear dichroism between 649-659 eV normalized by the ($I_\sigma + I_\pi$), ALD = $(I_\sigma - I_\pi)/(I_\sigma + I_\pi) \times 100\%$. A positive (or negative) ALD indicates a preferential occupation of $3z^2$–r^2 (or x^2–y^2) orbital.[20] By integrating the spectra in the range 649–659 eV (around the Mn L_2 edge), the area under the XLD

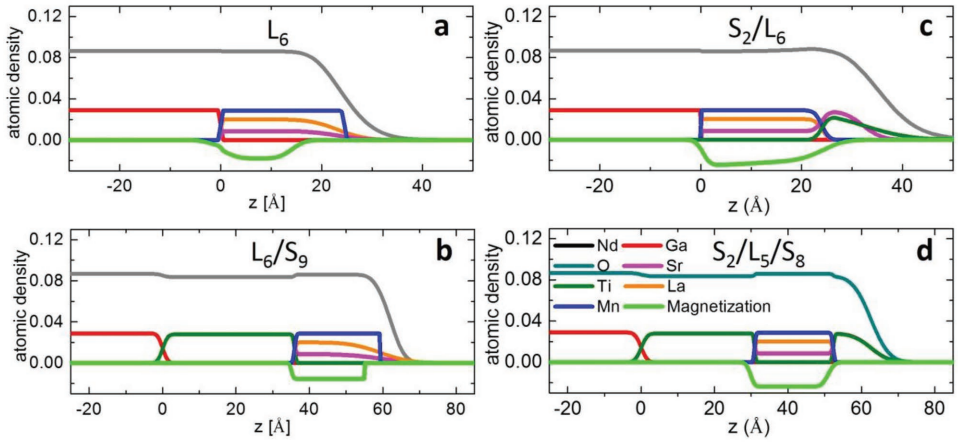

Figure 3. Stoichiometry and magnetic profiles for different LSMO films with/without STO buffer/capping layers. The depth profiles of the Ga, Ti, Mn, Nd, La, Sr, and O atomic concentration and Mn magnetization were measured at 20 K. The detailed stacking of the samples: a) L_6; b) L_6/S_9; c) S_2/L_6; d) $S_2/L_5/S_8$.

peak is obtained and plotted as a function of T_C for different films (see Figure 4c). The ALDs of all different films are ≈1%, indicating a very small orbital polarization with light preferential occupation of the $3z^2–r^2$ orbital. Since the XLDs were taken at 300 K, well above the T_C of LSMO films thinner than 30 uc (Figure 4c), therefore, the contribution of magnetization to XLD can be ruled out. A change of orbital polarization is not accompanied by any change of the Curie temperature. Therefore one can infer that the small degree of orbital polarization present plays a minor role in magnetic ordering when the lattice mismatch is relatively small.

It is noteworthy that the 6 uc LSMO has a smaller orbital polarization than thicker films. This indicates a competitive action of compressive strain and octahedral tilt on tetragonal distortions of the octahedra. Since the Mn—Mn distances in the (110) plane are locked-in by the NGO substrate, the tilting of the octahedra will increase the Mn—O bond length in the (110) plane, compensating the effect from compressive strain which tends to elongate the Mn—O bond in the direction normal to the interface. This effect subsides with increasing thickness, and hence orbital polarization will increase in thicker films. With a STO BL, the octahedral tilt disappears in ultrathin LSMO,[13]

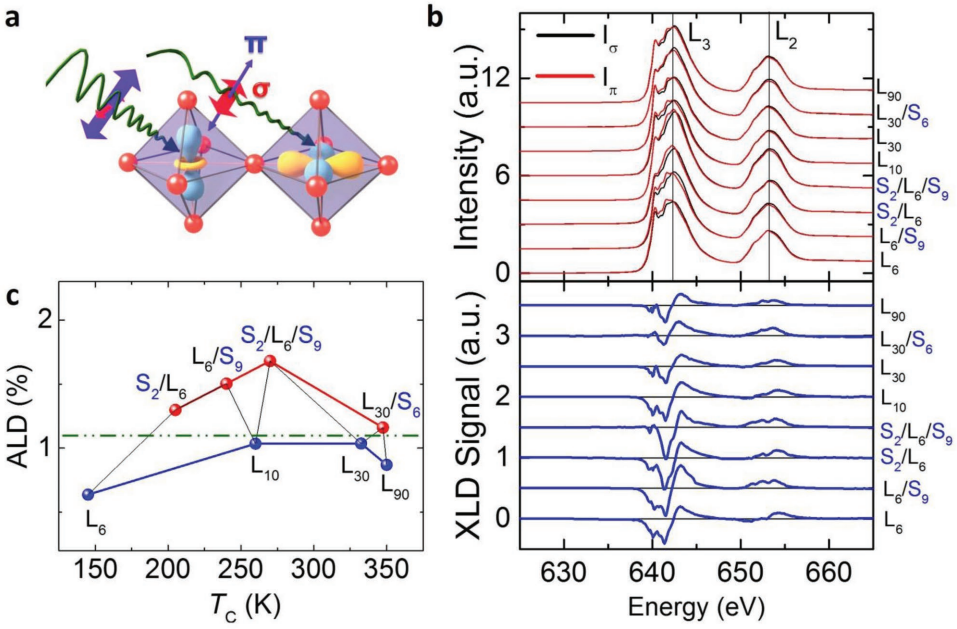

Figure 4. Orbital reconstruction probed by X-ray absorption spectroscopy. a) Sketch of the X-ray absorption measurement of $3z^2–r^2$ and $x^2–y^2$ orbital occupation by π- and σ-polarized lights, respectively. b) Polarized photons (in-plane σ, out of plane π) dependent XAS of Mn $L_{2,3}$ edge (top panel) and corresponding linear dichroism (bottom panel) of different LSMO films with/without STO buffer/capping layer. c) Integrated linear dichroism from 649–659 eV normalized by the $(I_\sigma + I_\pi)$ for LSMO films, ALD = $(I_\sigma - I_\pi)/(I_\sigma + I_\pi) \times 100\%$. All XLDs were measured at 300 K.

squeezing the in-plane Mn—O bond, resulting in an increased occupation of the $3z^2–r^2$ orbital in L_6/S_9 film as shown in Figure 4c. The STO CL is also found to enhance orbital polarization of both nonbuffered and buffered 6 uc LSMO, indicating a bulk like electronic structure at the surface layer, which can be connected to the recovery of surface magnetism as illustrated above by RSXR (see Figure 3). Although a large orbital polarization has been found to favor an antiferromagnetic insulating phase in largely strained LSMO/$DyScO_3$[40] and LSMO/$LaAlO_3$ films,[41] the orbital polarization in the LSMO films on NGO substrates seems to be so small that it plays only a minor role for the ferromagnetic ordering. Furthermore, the XAS results of different LSMO films (Figure 4b) show identical peak position of the Mn $L_{2,3}$ edge, indicating that a valence change does not play a significant role as well. Our previous cross-sectional STEM characterization and X-ray reciprocal space mapping also demonstrate an unchanged orthorhombic symmetry for different thicknesses of LSMO films on NGO (110).[13,14] Therefore, local bonding strength should play a central role and the ferromagnetic ordering of LSMO films grown on NGO is more likely determined by p–d hybridization.[33]

In fact, the relaxation of octahedral tilts can be connected to a spatial variation of p–d hybridization within LSMO as schematically illustrated in **Figure 5**a. With larger octahedral tilt, the overlap of the O-2p and Mn-3d orbitals is smaller. Due to the OOC effect, the Mn—O—Mn bond angle near the interface is close to the substrate Ga—O—Ga bond angle of (154°) as discussed above. This corresponds to the critical bond angle for the paramagnetic to ferromagnetic phase transition in $La_{2/3}R_{1/3}MnO_3$.[33] Furthermore, the tilting of the octahedra together with the compressive strain effect will elongate both the in-plane and out-of-plane Mn—O bonds as mentioned above, and thus the octahedral tilt and elongated Mn—O bond will cooperatively reduce the p–d hybridization and bandwidth as is demonstrated by first principle density functional theory calculations (see Table S1 and Figure S7 in the Supporting Information). Our Density Funtional Theory (DFT) calculations indicate that the bandwidth of the e_g orbital is reduced by 28% due to a decrease of the Mn—O—Mn bond angle from 180° to 151.5° while maintaining the Mn—O bond length. The reduction of bandwidth can be further promoted to 32% if the Mn—Mn distance is kept constant when changing the bond angle from 180° to 151.5°.

Experimentally, the effect of the octahedral tilt on the strength of p–d hybridization is directly measured by atomically resolved fine-structure changes at the O–K edge in electron energy loss spectroscopy (EELS). Figure 5b shows layer resolved spectra of the O–K edge spectrum taken from the individual layers across a nonbuffered LSMO film. There is a strong peak in the pre-edge region (528–531 eV), revealing that the holes introduced by Sr doping have a strong mixture of O-2p and Mn-3d character.[42,43] When getting closer to the LSMO/NGO interface, the prepeak intensity is found to decrease within the first 6 uc (see inset panel in Figure 5b), suggesting a weaker

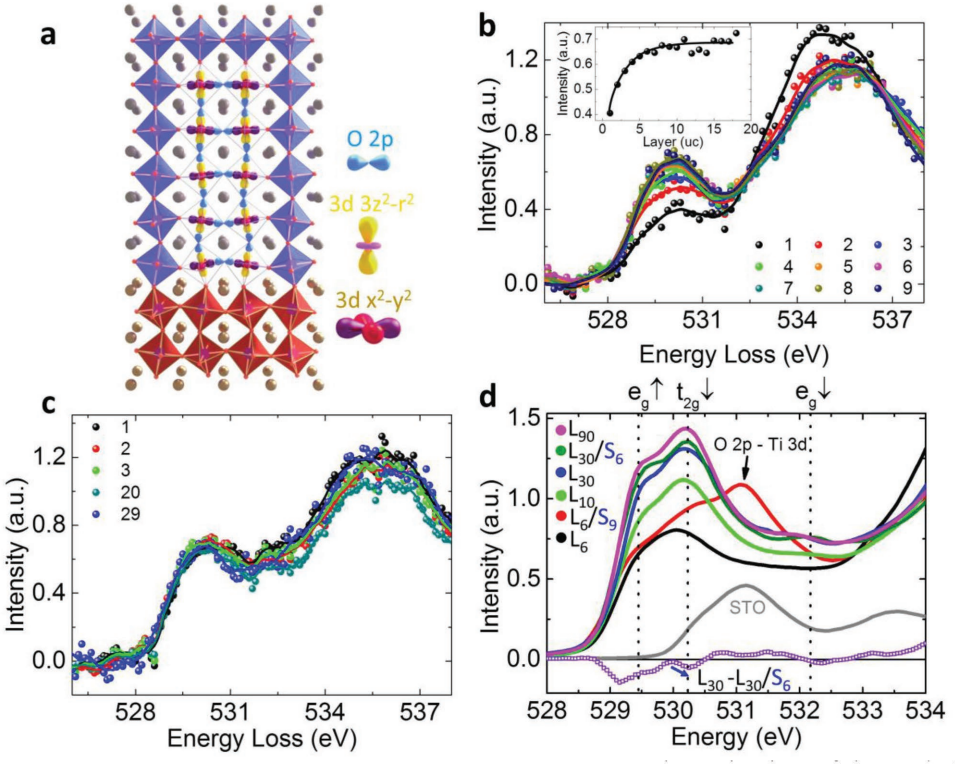

Figure 5. Mn-3d and oxygen-2p orbital hybridization. a) Schematic view of the evolution of the overlap of Mn-3d orbital with O-2p orbitals across the interface in the oxide heterostructure. Detailed O–K edge spectra of individual layers from EELS atomically resolved mapping for b) a 30 uc LSMO (L_{30}) and c) a buffered 30 uc LSMO (L_{30}/S_6). d) XAS O–K edge spectra of different LSMO films with/without STO buffer layer measured at 50 K. The gray curve is the O–K edge of a pure STO crystal. The open blue curve is the intensity difference between L_{30} and L_{30}/S_6.

O-2p and Mn-3d hybridization.[44,45] Although more occupancy of Mn e_g orbital will lead to a reduction of pre-edge intensity, it is not very significant $I(Mn^{3+})/I(Mn^{4+}) = 0.8$.[46] Furthermore, a sole valence effect is expected to induce a slightly higher intensity near the interface due to a small increase in hole doping of interfacial Mn. Therefore, the reduced pre-edge intensity arises from a structure variation (see also Figure S8 in the Supporting Information). The change of the orbital hybridization from the bulk region toward the interface agrees well with the schematic structure profile shown in Figure 5a. By introducing a STO BL, which has the effect of suppressing the MnO_6 octahedral tilt near the interface, the O–K edge becomes identical at the near-interface region than in bulk (see Figure 5c). We can conclude that a reduction of the p–d hybridization, which is a consequence of a change of the tilt of the MnO_6 octahedra, is at the origin of the reduction of T_C with decreasing film thickness.

The effect of thickness on the electronic structure of LSMO is further investigated by O K-edge XAS analysis of a series of buffered and nonbuffered films of various thickness. The pre-edge regions of the O K-edge of these different samples are shown in Figure 5d (for full spectra, see Figure S9 in the Supporting Information). At 50 K, three peaks at 529.5, 530, and 532 eV are observed in 90 uc LSMO film (L_{90}) and assigned to $e_g\uparrow$, $t_{2g}\downarrow$, and $e_g\downarrow$, respectively.[42] The L_{90} shows a spectrum quite similar to bulk crystalline LSMO,[42] indicating a bulk-dominated p–d hybridization in thick LSMO. For L_{30} film, which has lower T_C than bulk (see Figure 1d), the pre-edge has a lower intensity. However, a 6 uc STO BL can drive the pre-edge of 30 uc LSMO (L_{30}/S_6) to be similar to the one observed for a L_{90} film. As a consequence, the L_{30}/S_6 film behaves identically to a L_{90} film, e.g., same Curie temperature (see Figure 2a). For thinner 10 and 6 uc LSMO films, the reduced amount of absorption in the film relative to the substrate also reduces the pre-edge intensity, so the change of intensity cannot be directly interpreted for p–d hybridization. However, the different line shapes of the pre-edge still reflect a profound change of the Mn–O covalency. The most remarkable characteristic change of line shapes is the disappearance of the double-peak aspect of the pre-edge with reducing film thickness. The disappearance of this double peak is attributed to a loss of intensity of the first peak located at 529.5 eV ($e_g\uparrow$).[47,48] This is further suggested by a dip around the first peak in the $I(L_{30})-I(L_{30}/S_6)$ curve (see Figure 5d). The intensity of the third peak located at 530 eV ($e_g\downarrow$) is reduced as well as the thickness is decreased. Reduced intensity of $e_g\uparrow$ and $e_g\downarrow$ peaks has been interpreted as a signature of electron localization and more ionic environment of Mn, resulting in less hybridization between O and Mn.[45,48] Moreover, the double peak feature is recovered in buffered 6 uc LSMO film (L_6/S_9) (see Figure 5d). A spectrum from a pure STO crystal verifies that the STO buffer layer does not contribute to the prepeak region and only adds a bump at higher energies. This fact underlines the important role of structure distortion in p–d hybridization.

3. Conclusion

In conclusion, octahedral relaxation leading to a change of p–d hybridization driven by interfacial OOC appears to be the strongest factor in thickness related variations of magnetic and transport properties in epitaxial LSMO films on NGO substrates. Our study demonstrates that the reconstructed octahedral rotation pattern due to the OOC effect at the interface is a nontrivial factor of perovskite oxide interfaces and causes a thickness dependent orbital hybridization effect. Although LSMO has been used as a prototype material for this study, the results presented here can be applied to understand thickness related properties variations in many other correlated oxide perovskite systems and have deep implications for understanding emergent functionalities in those complex systems. Our results further reaffirm the important role of mixed transition metal 3d and oxygen 2p character in TMOs[2] and address the advantage of heterostructures whose interfaces allow us to freely control p–d orbital hybridization in the prospect of controlling and tailoring functionalities. The octahedral relaxation can be modified or even suppressed by engineering the interface octahedral rotation network, e.g., inserting a nontilted STO buffer layer, which has the effect of enhancing magnetism. The magnetic dead layer can be eliminated by introducing STO capping layers, making LSMO very promising for near-future spintronic applications. The strong impact of a STO buffer layer on the properties of both ultrathin and thick LSMO films indicate an efficient way to engineer functionalities via local control of OOC. The capability to pattern such buffer and capping layers, as demonstrated here, also allows us to develop new types of devices with smaller length scales and new type of junctions. The revealed origin of thickness-properties correlation discussed here paves the way toward scaling down of correlated oxide systems in order to achieve smaller scale new full oxide electronics.

4. Experimental Section

The STO and LSMO layers were grown by pulsed laser deposition (PLD) at 680 °C on atomically flat NGO (110) substrates from a single crystalline STO target and a stoichiometric $La_{2/3}Sr_{1/3}MnO_3$ ceramic target, respectively. The PLD used a KrF excimer laser operating at 248 nm and at a repetition rate of 2 Hz. The atomically flat NGO substrates were obtained by buffered HF chemical etching and subsequent annealing at 1050 °C for 4 h.[49] The oxygen partial pressure during growth was 0.2 mbar. The laser energy fluences for the growth of LSMO and STO were 0.6 and 1 J cm^{-2}, respectively. The growth process was monitored by reflection high-energy electron diffraction, which confirmed the layer by layer characteristic growth. The surfaces of the films were atomically flat as confirmed by atomic force microscopy. For patterned LSMO sample, the patterned STO layers were fabricated by using a shadow mask during growth, while there was no shadow mask for the growth of LSMO. This growth process ensured that the LSMO at different regions experienced same condition.

Transport and magnetism were characterized by quantum design physics properties measurement system and VSM, respectively. The magnetization was obtained by subtracting the NGO paramagnetic signal.[13] The lattice parameters of the thin films were characterized by PANalytical-X'Pert materials research diffractometers at high resolution mode. Atomic scale characterization of the lattice structure using ABF-STEM imaging at 300 kV and EELS were performed on the Quant-EM instrument at the University of Antwerp. For STEM-EELS experiments, the beam was monochromated to achieve a 100 meV energy resolution and the microscope operated at 120 kV to reduce beam-damage. Cross-sectional cuts of the samples along the NGO [1-10] direction were prepared using a FEI Helios 650 dual-beam focused ion beam device.

Stoichiometry and magnetic profiles were probed by using resonant RSXR. The RSXR experiments were performed using an in-vacuum 4-circle diffractometer at the resonant elastic and inelastic X-ray scattering beamline at Canadian light source in Saskatoon, Canada. The beamline has a flux of 5×10^{12} photon s^{-1} and photon energy resolution $\Delta E/E$ of $\approx 10^{-4}$. The base pressure of the diffractometer chamber was kept lower than 10^{-9} Torr. The samples were aligned with their surface normal in the scattering plane and measured at a temperature of 20 K. The measurements were carried out in the specular reflection geometry with several nonresonant photon energies as well as energies at the Mn $L_{2,3}$ resonance (≈635–660 eV). XLD was performed to investigate the 3d x^2-y^2 and $3z^2-r^2$ orbital occupancy by using σ polarized (polarization vector near perpendicular to the surface) and π polarized (polarization vector in the surface) photons. XAS of oxygen K-edge was measured with the photon polarized along [001] axis of NGO.

The mapping of polar Kerr signal with spatial resolution of 2 µm was performed on a scanning Sagnac interferometer at University of California, Irvine, USA. A magnetic field of 0.2 T was applied along surface normal direction to cant the magnetization along out-of-plane direction. The Curie temperature was defined as the point in the Kerr signal versus temperature of maximum curvature.

Supporting Information

Supporting Information is available from the Wiley Online Library or from the author.

Acknowledgements

M.H., G.K., and G.R. acknowledge funding from DESCO program of the Dutch Foundation for Fundamental Research on Matter (FOM) with financial support from the Netherlands Organization for Scientific Research (NWO). This work was funded by the European Union Council under the 7th Framework Program (FP7) Grant No. NMP3-LA-2010-246102 IFOX. J.V. and S.V.A. acknowledge financial support from the Research Foundation Flanders (FWO, Belgium) through project fundings (Grant Nos. G.0044.13N, G.0374.13N, G.0368.15N, and G.0369.15N). The Qu-Ant-EM microscope was partly funded by the Hercules fund from the Flemish Government. N.G. acknowledges funding from the European Research Council under the 7th Framework Program (FP7), ERC Starting Grant No. 278510 VORTEX. N.G., J.G., S.V.A., and J.V. acknowledge financial support from the European Union under the Seventh Framework Program under a contract for an Integrated Infrastructure Initiative (Reference No. 312483-ESTEEM2). The Canadian work was supported by NSERC and the Max Planck-UBC Centre for Quantum Materials. Some experiments for this work were performed at the Canadian Light Source, which was funded by the Canada Foundation for Innovation, NSERC, the National Research Council of Canada, the Canadian Institutes of Health Research, the Government of Saskatchewan, Western Economic Diversification Canada, and the University of Saskatchewan.

Received: December 20, 2016
Revised: January 25, 2017
Published online:

[1] E. Dagotto, *Science* **2005**, *309*, 257.
[2] J. Zaanen, G. A. Sawatzky, J. W. Allen, *Phys. Rev. Lett.* **1985**, *55*, 418.
[3] M. Imada, A. Fujimori, Y. Tokura, *Rev. Mod. Phys.* **1998**, *70*, 1039.
[4] A. V. Boris, Y. Matiks, E. Benckiser, A. Frano, P. Popovich, V. Hinkov, P. Wochner, M. Castro-Colin, E. Detemple, V. K. Malik, C. Bernhard, T. Prokscha, A. Suter, Z. Salman, E. Morenzoni, G. Cristiani, H.-U. Habermerier, B. Keimer, *Science* **2011**, *332*, 937.
[5] P. D. C. King, H. I. Wei, Y. F. Nie, M. Uchida, C. Adamo, S. Zhu, X. He, I. Božović, D. G. Schlom, K. M. Shen, *Nat. Nanotechnol.* **2014**, *9*, 443.
[6] K. Yoshimatsu, T. Okabe, H. Kumigashira, S. Okamoto, S. Aizaki, A. Fujimori, M. Oshima, *Phys. Rev. Lett.* **2010**, *104*, 147601.
[7] X. R. Wang, C. J. Li, T. R. Paudel, D. P. Leusink, M. Hoek, N. Poccia, A. Vailionis, T. Venkatesan, J. M. D. Coey, E. Y. Tsymbal, Ariando, H. Hilgenkamp, *Science* **2015**, *349*, 6249.
[8] G. Koster, L. Klein, W. Siemons, G. Rijnders, J. S. Dodge, C.-B. Eom, D. H. A. Blank, M. R. Beasley, *Rev. Mod. Phys.* **2012**, *84*, 253.
[9] J. Junquera, P. Ghosez, *Nature* **2003**, *422*, 506.
[10] M. Huijben, L. W. Martin, Y.-H. Chu, M. B. Holcomb, P. Yu, G. Rijnders, D. H. A. Blank, R. Ramesh, *Phys. Rev. B* **2008**, *78*, 094413.
[11] J. M. Rondinelli, S. J. May, J. W. Freeland, *MRS Bull.* **2012**, *37*, 261.
[12] D. Kan, R. Aso, R. Sato, M. Haruta, H. Kurata, Y. Shimakawa, *Nat. Mater.* **2016**, *15*, 432.
[13] Z. L. Liao, M. Huijben, Z. Zhong, N. Gauquelin, S. Macke, R. J. Green, S. Van Aert, J. Verbeeck, G. Van Tendeloo, K. Held, G. A. Sawatzky, G. Koster, G. Rijnders, *Nat. Mater.* **2016**, *15*, 425.
[14] Z. L. Liao, R. J Green, N. Gauquelin, S. Macke, L. Li, J. Gonnissen, R. Sutarto, E.P Houwman, Z. Zhong, S. Van Aert, J. Verbeeck, G. A. Sawatzky, M. Huijben, G. Koster, G. Rijnders, *Adv. Funct. Mater.* **2016**, *26*, 6627.
[15] R. Gao, Y. Q. Dong, H. Xu, H. Zhou, Y. K. Yuan, V. Gopalan, C. Gao, D. D. Fong, Z. H. Chen, Z. L. Luo, L. W. Martin, *ACS Appl. Mater. Interfaces* **2016**, *8*, 14871.
[16] Y. Tokura, Y. Tomioka, *J. Magn. Magn. Mater.* **1999**, *200*, 1.
[17] J.-H. Park, E. Vescovo, H.-J. Kim, C. Kwon, R. Ramesh, T. Venkatesan, *Nature* **1998**, *392*, 794.
[18] A. Tebano, C. Aruta, S. Sanna, P. G. Medaglia, G. Balestrino, A. A. Sidorenko, R. De Renzi, G. Ghiringhelli, L. Braicovich, V. Bisogni, N. B. Brookes, *Phys. Rev. Lett.* **2008**, *100*, 137401.
[19] M. B. Lepetit, B. Mercey, C. Simon, *Phys. Rev. Lett.* **2012**, *108*, 087202.
[20] D. Pesquera, G. Herranz, A. Barla, E. Pellegrin, F. Bondino, E. Magnano, F. Sánchez, J. Fontcuberta, *Nat. Commun.* **2012**, *3*, 1189.
[21] H. Boschker, J. Verbeeck, R. Egoavil, S. Bals, G. Van Tendeloo, M. Huijben, E. P. Houwman, G. Koster, D. H. A. Blank, G. Rijnders, *Adv. Funct. Mater.* **2012**, *22*, 2235.
[22] H. Dulli, P. A. Dowben, S.-H. Liou, E. W. Plummer, *Phys. Rev. B* **2000**, *62*, R14629.
[23] F. Sandiumenge, J. Santiso, L. Balcells, Z. Konstantinovic, J. Roqueta, A. Pomar, J. P. Espinós, B. Martínez, *Phys. Rev. Lett.* **2013**, *110*, 107206.
[24] J.-S. Lee, D. A. Arena, P. Yu, C. S. Nelson, R. Fan, C. J. Kinane, S. Langridge, M. D. Rossell, R. Ramesh, C.-C. Kao, *Phys. Rev. Lett.* **2010**, *105*, 257204.
[25] H. Yamada, Y. Ogawa, Y. Ishii, H. Sato, M. Kawasaki, H. Akoh, Y. Tokura, *Science* **2004**, *305*, 646.
[26] A. Vailionis, H. Boschker, Z. L. Liao, J. R. A. Smit, G. Rijnders, M. Huijben, G. Koster, *Appl. Phys. Lett.* **2014**, *105*, 131906.
[27] L. F. Kourkoutis, J. H. Song, H. Y. Hwang, D. A. Muller, *Proc. Natl. Acad. Sci. USA* **2010**, *107*, 11682.
[28] Z. Fang, I. V. Solovyev, K. Terakura, *Phys. Rev. Lett.* **2000**, *84*, 3169.
[29] Y. Konishi, Z. Fang, M. Izumi, T. Manako, M. Kasai, H. Kuwahara, M. Kawasaki, K. Terakura, Y. Tokura, *J. Phys. Soc. Jpn.* **1999**, *68*, 3790.
[30] J. A. Mundy, Y. Hikita, T. Hidaka, T. Yajima, T. Higuchi, H. Y. Hwang, D. A. Muller, L. F. Kourkoutis, *Nat. Commun.* **2014**, *5*, 3464.
[31] A. Bhattacharya, S. J. May, S. G. E. te Velthuis, M. Warusawithana, X. Zhai, B. Jiang, J.-M. Zuo, M. R. Fitzsimmons, S. D. Bader, J. N. Eckstein, *Phys. Rev. Lett.* **2008**, *100*, 257203.
[32] P. G. Radaelli, G. Iannone, M. Marezio, H. Y. Hwang, S.-W. Cheong, J. D. Jorgensen, D. N. Argyriou, *Phys. Rev. B* **1997**, *56*, 8265.

[33] J. L. Garcia-Munoz, J. Fontcuberta, M. Suaaidi, X. Obradors, *J. Phys.: Condens. Matter* **1996**, *8*, L787.
[34] A. J. den Dekker, S. Van Aert, A. van den Bos, D. Van Dyck, *Ultramicroscopy* **2005**, *104*, 83.
[35] S. Van Aert, A. J. den Dekker, A. van den Bos, D. Van Dyck, J. H. Chen, *Ultramicroscopy* **2005**, *104*, 107.
[36] H. Boschker, M. Huijben, A. Vailionis, J. Verbeeck, S. Van Aert, M. Luysberg, S. Bals, G. Van Tendeloo, E. P. Houwman, G. Koster, D. H. A. Blank, G. Rijnders, *J. Phys. D: Appl. Phys.* **2011**, *44*, 205001.
[37] J. Xia, P. T. Beyersdorf, M. M. Fejer, A. Kapitulnik, *Appl. Phys. Lett.* **2006**, *89*, 062508.
[38] S. Macke, A. Radi, J. E. Hamann-Borrero, A. Verna, M. Bluschke, S. Brück, E. Goering, R. Sutarto, F. Z. He, G. Cristiani, M. Wu, E. Benckiser, H.-U. Habermeier, G. Logvenov, N. Gauquelin, G. A. Botton, A. P. Kajdos, S. Stemmer, G. A. Sawatzky, M. W. Haverkort, B. Keimer, V. Hinkov, *Adv. Mater.* **2014**, *26*, 6554.
[39] D. P. Kumah, A. S. Disa, J. H. Ngai, H. H. Chen, A. Malashevich, J. W. Reiner, S. Ismail-Beigi, F. J. Walker, C. H. Ahn, *Adv. Mater.* **2014**, *26*, 1935.
[40] B. M. Wang, L. You, P. Ren, X. M. Yin, Y. Peng, B. Xia, L. Wang, X. J. Yu, S. M. Poh, P. Yang, G. L. Yuan, L. Chen, A. Rusydi, J. L. Wang, *Nat. Commun.* **2013**, *4*, 2778.
[41] A. Tebano, C. Aruta, P. G. Medaglia, F. Tozzi, G. Balestrino, A. A. Sidorenko, G. Allodi, R. De Renzi, G. Ghiringhelli, C. Dallera, L. Braicovich, N. B. Brookes, *Phys. Rev. B* **2006**, *74*, 245116.
[42] E. Pellegrin, L. H. Tjeng, F. M. F. de Groot, R. Hesper, G. A. Sawatzky, Y. Moritomo, Y. Tokura, *J. Electron Spectrosc. Relat. Phenom.* **2013**, *86*, 115.
[43] H. Wadati, A. Maniwa, A. Chikamatsu, H. Kumigashira, M. Oshima, T. Mizokawa, A. Fujimori, G. A. Sawatzky, *Phys. Rev. B* **2009**, *80*, 125107.
[44] F. M. F. de Groot, M. Gnom, J. C. Fuggle, J. Ghijsen, G. A. Sawatzky, H. Petersen, *Phys. Rev. B* **1989**, *40*, 5715.
[45] J. Suntivich, W. T. Hong, Y.-L. Lee, J. M. Rondinelli, W. L. Yang, J. B. Goodenough, B. Dabrowski, J. W. Freeland, Y. Shao-Horn, *J. Phys. Chem. C* **2014**, *118*, 1856.
[46] J. Verbeeck, O. I. Lebedev, G. Van Tendeloo, J. Silcox, B. Mercey, M. Hervieu, A. M. Haghiri-Gosnet, *Appl. Phys. Lett.* **2001**, *79*, 2037.
[47] J.-H. Park, T. Kimura, Y. Tokura, *Phys. Rev. B* **1998**, *58*, R13330(R).
[48] N. Mannella, C. H. Booth, A. Rosenhahn, B. C. Sell, A. Nambu, S. Marchesini, B. S. Mun, S.-H. Yang, M. Watanabe, K. Ibrahim, E. Arenholz, A. Young, J. Guo, Y. Tomioka, C. S. Fadley, *Phys. Rev. B* **2008**, *77*, 125134.
[49] V. Leca, D. H. A. Blank, G. Rijnders, *arXiv* **2012**, *1202*, 2256.